

SCIENTIFIC REPORTS

OPEN

Reduced partitioning of plastic strain for strong and yet ductile precipitate-strengthened alloys

R. D. Jones¹, F. Di Gioacchino¹, H. Lim², T. E. J. Edwards¹, C. Schwalbe¹, C. C. Battaile² & W. J. Clegg¹

When a material that contains precipitates is deformed, the precipitates and the matrix may strain plastically by different amounts causing stresses to build up at the precipitate-matrix interfaces. If premature failure is to be avoided, it is therefore essential to reduce the difference in the *plastic* strain between the two phases. Here, we conduct nanoscale digital image correlation to measure a new variable that quantifies this plastic strain difference and show how its value can be used to estimate the associated interfacial stresses, which are found to be approximately three times greater in an Fe-Ni₂AlTi steel than in the more ductile Ni-based superalloy CMSX-4[®]. It is then demonstrated that decreasing these stresses significantly improves the ability of the Fe-Ni₂AlTi microstructure to deform under tensile loads without loss in strength.

Many alloys used in the most demanding structural applications are made up of nanosized precipitates dispersed within a metallic matrix^{1–11}. The precipitates strengthen the solid by resisting the movement of the defects that give rise to plastic deformation. However, if there is a difference in *plastic* strain between the matrix and the precipitates, stresses are generated at the precipitate-matrix interfaces that can lead to premature failure^{12–14}. While X-ray and neutron diffraction techniques have been used to quantify the elastic strain difference between the two phases^{15–20}, it has not so far been possible to measure this plastic strain difference in these materials. The present paper demonstrates a way of doing this and describes how to estimate the interfacial stresses from such measurements. Also, it shows that reducing these stresses improves the usually poor ductility of very strong precipitate-matrix microstructures. This is significant, as the latter must be able to deform plastically under tensile loads to prevent the nucleation of damage and the propagation of cracks²¹.

The strain that accumulates at the surface of a testpiece can be quantified using the expression for the maximum shear strain, γ_{max} , which is a positive scalar-valued function of the strain components, as shown in the Methods section. As the elastic contribution to the total strain is negligible at large deformation, the partitioning of plastic strain can be simply expressed as the difference between the mean values of γ_{max} in the matrix, $\langle \gamma_{max}^M \rangle$, and the precipitates, $\langle \gamma_{max}^P \rangle$:

$$p_{plastic} = \langle \gamma_{max}^M \rangle - \langle \gamma_{max}^P \rangle \quad (1)$$

The value of $p_{plastic}$ is positive if the strain is less in the precipitates than in the matrix and negative if it is greater in the precipitates.

To measure $\langle \gamma_{max}^M \rangle$ and $\langle \gamma_{max}^P \rangle$ in Equation 1, one must be able to map strains at the length scale of the precipitates. This can be achieved using digital image correlation (DIC) to track the displacement of fine speckles applied onto the area of interest before testing²². The speckles must be present in both the precipitates and the matrix channels, which can be even narrower than the precipitate size when the volume fraction occupied by the matrix is greater than about one-eighth (having considered cubic shaped precipitates). After mapping the strains, masking of the precipitates is required to group the strain data by phase type. Therefore, the precipitates must be visible in the same images used for DIC. In precipitate-strengthened alloys with nanosized precipitates, the speckles must then be of nanoscale size and applied with a method that distributes them evenly (i.e. not randomly) across

¹Gordon Laboratory, Department of Materials Science and Metallurgy, The University of Cambridge, 27 Charles Babbage Rd, Cambridge, CB3 0FS, UK. ²Department of Computational Materials and Data Science, Sandia National Laboratories, Albuquerque, NM, 87185, United States. Correspondence and requests for materials should be addressed to F.D.G. (email: f.digioacchino@gmail.com)

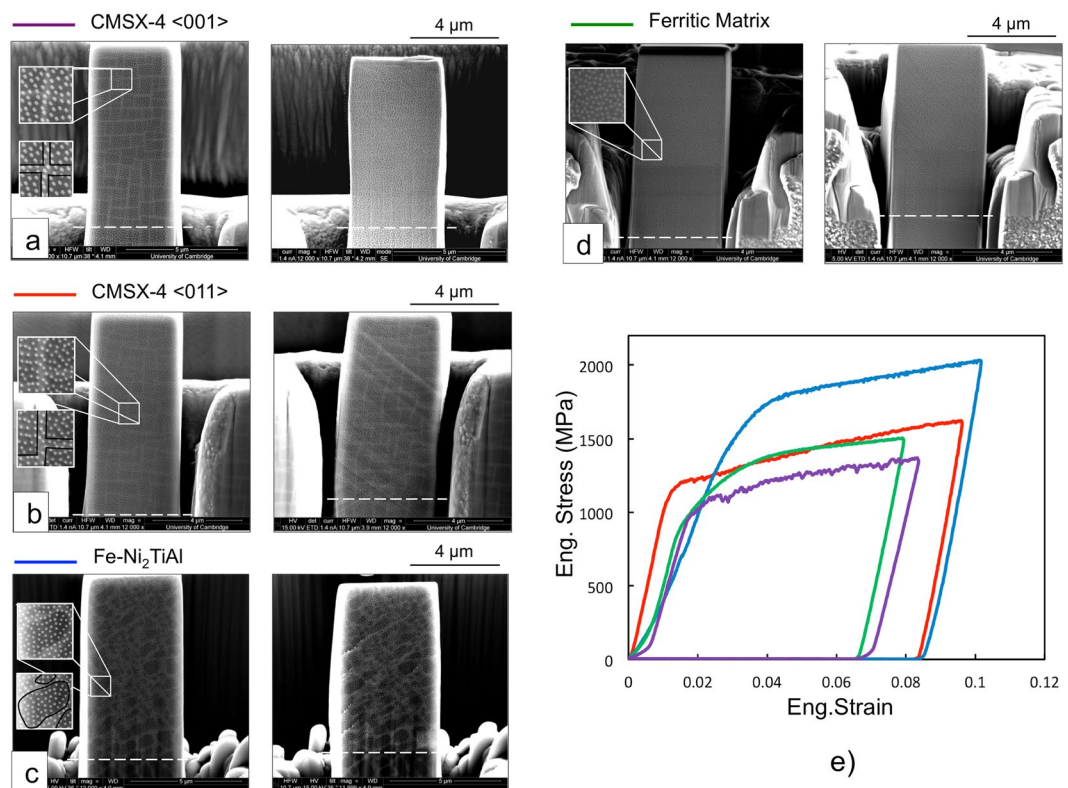


Figure 1. (a–d) SEM images of the pillars before (left) and after ~ 0.1 compressive strain (right) with enlarged areas showing the Pt speckle pattern. The white dashed lines, which translate with the base of the pillars, help to visualise the macroscopic strain. The lateral offset of the top part of the CMSX-4 $\langle 011 \rangle$ pillar is attributed to the combination of single slip (as seen in the strain map) and the sliding at the pillar-indenter interface. (e) Stress-strain curves.

the area to maximise both the spatial resolution and the accuracy of the DIC. This contrasts with the less stringent requirements to be met when characterising the distribution of plastic strain in polycrystalline multiphase alloys that show comparatively large and distant second phase grains or particles^{23–30}.

Example of high resolution DIC measurements of plastic strain in the Ni-based precipitate-strengthened alloy René 88DT can be found in the work of Stinville *et al.*^{31,32} In this, the speckles pattern is created by carving the precipitates exposed at the surface of the sample using etchants. As each carved precipitate represents a speckle, the relative displacements of the speckles obtained by DIC can only be used to quantify the deformation of the matrix material. One can then envisage the use of remodelling of deposited films to create a nanoscale and non-random pattern in a non-destructive fashion^{33,34}. However, the residues of deposited material between the speckles would not allow for the visualization of the underlining precipitates.

Here, we use the nanoscale DIC method recently developed to accurately map strains in small-scale testing^{35–37} to measure $p_{plastic}$ at room temperature in two precipitate-strengthened alloys, the single crystal Ni-based superalloy, CMSX-4[®], and an Fe-Ni₂AlTi steel. CMSX-4 is widely used for turbine blades in gas turbine engines and automotive turbochargers. It contains a volume fraction of ~ 0.7 of γ' -Ni₃Al, which are ordered precipitates embedded in a Ni-based γ -matrix¹ of same crystallographic orientation (coherent precipitates). The Fe-Ni₂AlTi steel shows an analogous microstructure with a ~ 0.5 volume fraction of coherent Ni₂AlTi β' -precipitates in an Fe-based β -matrix. These steels have been proposed for applications in supercritical steam turbines and yet their poor ductility has been preventing their practical use⁴.

Measurements of Plastic Strain Partitioning

To measure $p_{plastic}$ in CMSX-4 and at the same time demonstrate its independence of the loading direction, two CMSX-4 micropillars were compressed along different crystallographic directions ($\langle 001 \rangle$ and $\langle 011 \rangle$). A third micropillar was compressed to measure $p_{plastic}$ in the Fe-Ni₂AlTi steel. A fourth micropillar was milled from the ferritic matrix material and tested for comparison.

The secondary electron images of the four micropillars with their speckle pattern before and after compression are shown in Fig. 1a–d. As shown in the enlarged areas, the ~ 40 nm sized and evenly distributed speckles could be imaged in high contrast while also imaging the precipitates. Table 1 includes the estimates of the average size, spacing and volume fraction of the precipitates.

The stress-strain curves of the micropillar compression tests in Fig. 1e give yield stresses of the order of 1000 MPa and 1100 MPa for the CMSX-4 $\langle 010 \rangle$ and CMSX-4 $\langle 011 \rangle$, 1500 MPa for the Fe-Ni₂AlTi and 1000 MPa for the ferritic matrix only. As shown in Methods, these values were multiplied by the Schmid factors to estimate

Alloy	Vol. Fr.	Size (nm)	Spacing (nm)	Misfit (%)	$\langle \gamma_{max}^M \rangle$	$\langle \gamma_{max}^P \rangle$	$p_{plastic}$	G_M (GPa)	τ_B (MPa)
CMSX-4 [010]	0.71	510	160	—	0.1418	0.1450	−0.0032	123.4	280
CMSX-4 [011]	“	“	“	—	0.1442	0.1470	−0.0028	“	245
Fe-Ni ₂ AlTi	0.51	340	330	1.5	0.1354	0.1224	0.0130	116.5	772
+1.4 at.% Mo	0.47	150	160	1.1	0.1052	0.1032	0.0020	“	108
+3.3 at.% Mo	0.45	89	110	0.8	0.1282	0.1288	−0.0006	“	31

Table 1. Microstructural parameters, strain partitioning $p_{plastic}$ and back stress τ_B . The elastic constants are taken from Meyers *et al.*³⁸.

the critical resolved shear stresses. For CMSX-4, a mean value of ~460 MPa is obtained, which is similar to that reported in previous micropillar compression tests³⁹. Meanwhile, the Fe-Ni₂AlTi has a much higher critical stress of ~740 MPa. Without the precipitates, i.e. in the ferritic matrix micropillar, this decreases to ~480 MPa, in line with literature values of quenched low-alloy steels⁴⁰.

The SEM images in the four sets in Fig. 1 were digitally correlated to map the strains across the micropillars. The location of the precipitates was later identified in the maps to extract $\langle \gamma_{max}^M \rangle$ and $\langle \gamma_{max}^P \rangle$ in Equation 1, Table 1. The derivation of the experimental error of ~0.0008 associated with the noise in the acquisition of these images is described in the Methods section. To ensure meaningful comparison, measurements were taken over areas that had undergone similar macroscopic strains.

The maps of γ_{max} for the $\langle 001 \rangle$ and the $\langle 011 \rangle$ oriented CMSX-4 micropillars with an outline of the precipitates are shown in Fig. 2a and b, respectively. The strain accumulates along slip bands that align with the traces of the $\{111\}\langle 011 \rangle$ slip systems of highest resolved shear stress and are ~0.25 μm apart, i.e. less than the precipitate size. The shear strain varies along these bands, for instance between ~0.32 and ~0.40 in the most intense band in the strain map of Fig. 2a, with no apparent strain difference between the two phases. However, negative values of $p_{plastic} = -0.0032$ and $p_{plastic} = -0.0028$ measured for the $\langle 001 \rangle$ and $\langle 011 \rangle$ oriented micropillars, respectively, show that the precipitate phase has strained more than the matrix phase. This result provides evidence in support of early studies⁴¹ and more recent neutron diffraction measurements¹⁶ that are consistent with the precipitate phase of CMSX-4 being the soft phase at room temperature. Also, the relatively small difference between the two values, which is within the measurement uncertainty, suggests that the loading direction has no major effect on the partitioning of plastic strain.

The γ_{max} map of the Fe-Ni₂AlTi steel in Fig. 2c shows slip bands on the $\{011\}\langle 111 \rangle$ system with the highest resolved shear stress. Many precipitates including the large ones highlighted by white arrows shear with the matrix. However, some large precipitates appear to resist shearing by stopping or deflecting slip bands, as non-deformable particles do^{42,43}. This increases the average slip band spacing to ~0.38 μm , a value which is nearly twice the ~0.24 μm measured for the micropillar of the matrix material, Fig. 2d. These precipitates can be easily identified on the map as maximum shear strains of ~0.48 accumulate in the matrix material that surrounds them. This gives a positive $p_{plastic} = 0.0130$, the magnitude of which is thus more than four times that measured for CMSX-4.

Interfacial Back Stresses for the Case of Deformable Particles

Coherency of the precipitates with the matrix in precipitate-strengthened alloys simplifies the treatment of the incompatibility of plastic deformation between the two phases and the derivation of the associated interfacial stresses using analytical models. Here, we propose an extension of the Ashby model¹² for hard (i.e. non-deformable) particles to the case of (coherent) sheareable particles.

Taking a unit volume of particle-matrix material, Ashby imagined removing the particle before deformation so that the hole left behind would be free to change shape together with the matrix, Fig. 3a (left). This gives rise to a mismatch in the geometry of the undeformed particle and the hole. Upon reinsertion, a flow of dislocations must then displace the matrix around the particle to prevent any overlap or detachment of material at the particle-matrix interface, Fig. 3a (right). These so-called geometrically necessary dislocations (GNDs)⁴⁴ would pile-up against the precipitate, exerting a back stress that inhibits further slip in the matrix. Although these stresses strengthen the solid, their build-up promotes cavitation at the particle-matrix interfaces under tensile loads, causing internal fracture in particles with large aspect ratios¹⁴.

There is no unique arrangement of GNDs that restores the hole to its original shape. Figure 3 illustrates the particular case in which this is achieved by inserting n prismatic loops of Burgers vector b either side of a non-deformable cubic particle of size d . Taking l' as the length of each prismatic column and considering isotropic elastic behaviour of the matrix material, Ashby estimated the maximum shear component of the back stress at the surface of the particle, τ_B , to be of the order of $\tau_B = \frac{G_M n b}{l'}$, where G_M is the shear modulus of the matrix (note that a different expression, which includes the square root of the estimated dislocation density, has been given for this stress in Brown and Stobbs⁴⁵). He then linked l' to the precipitate volume fraction $f = \frac{d}{l'}$ and obtained:

$$\tau_B = G_M f \frac{n b}{d} \quad (2)$$

Geometry shows that the excess volume of matrix material to be inserted or removed by prismatic glide either side of the particle is $\Delta V = d \Delta A = 0.5 V_p \gamma_M = 0.5 d^3 \gamma_M$, where ΔA is the area highlighted in red in Fig. 3a and

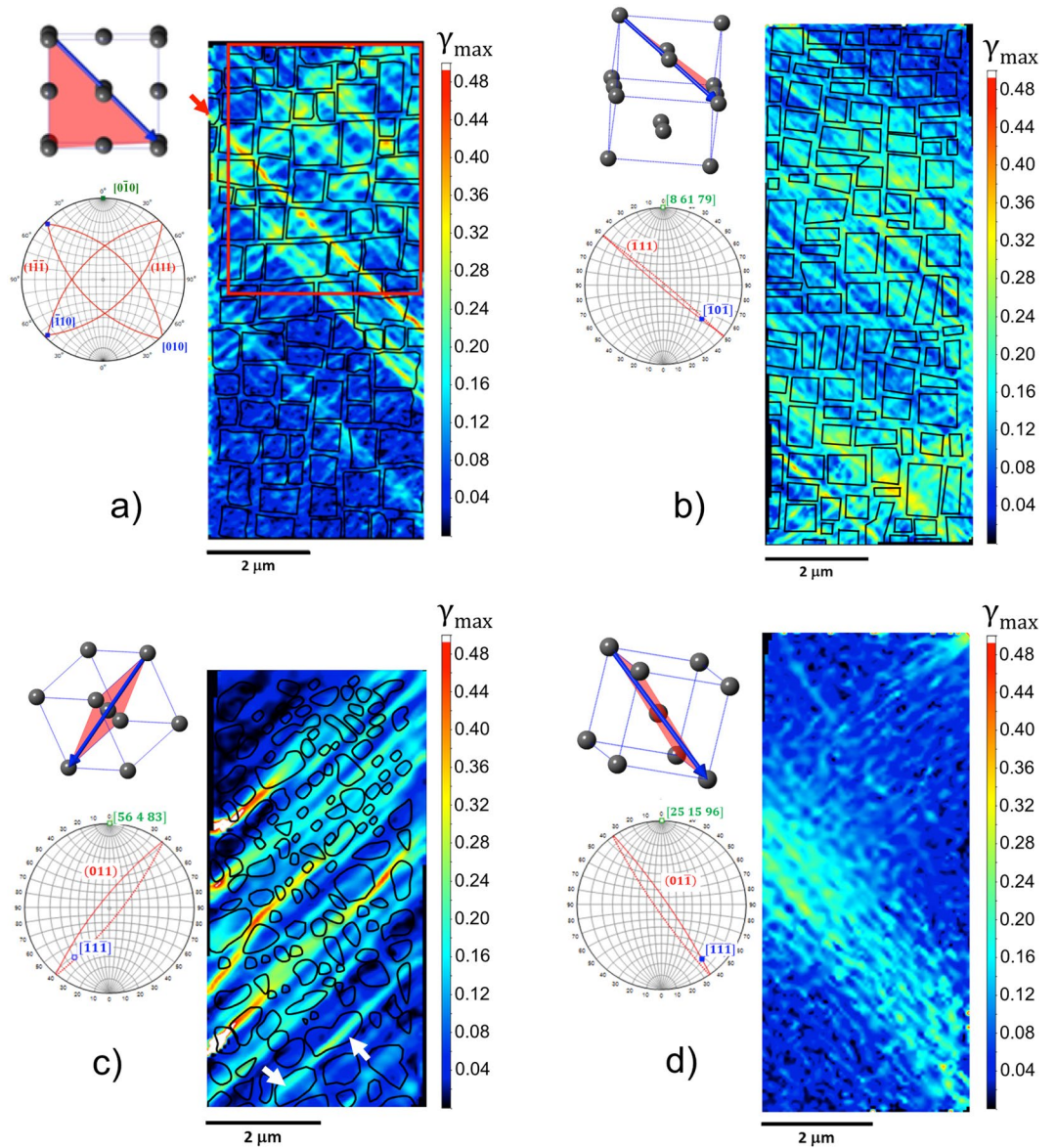


Figure 2. Maximum shear strain maps of the four micropillars with outline of the precipitates. (a) $\langle 001 \rangle$ oriented CMSX-4 micropillar. The red line outlines the area for which $p_{plastic}$ has been measured (b) Near (011) oriented CMSX-4 micropillar. (c) Fe-Ni₂AlTi micropillar. (d) Ferritic matrix-only micropillar, i.e. without Ni₂AlTi precipitates. Unit cells and stereograms show the crystallographic orientation and active slip systems in each pillar. The compression axis is shown in green, the slip planes in red and the slip directions in blue.

$V_p = d^3$ is the volume occupied by the particle. Therefore, taking $0.5d^2$ as the area bounded by each loop, the excess volume is $\Delta V = 0.5nb d^2$. Combining the two expressions for ΔV above gives:

$$n = \frac{\gamma_M d}{b} \tag{3}$$

Finally, substituting Equation 3 for n in Equation 2 gives:

$$\tau_B = G_M f \gamma_M \tag{4}$$

Equation 4 cannot be used to evaluate τ_B in materials that contain deformable particles because the excess volume ΔV would also depend on γ_p . However, γ_p can now be experimentally measured. One can then simply imagine having sheared the particle by such known amount before reinserting it, as shown in Fig. 3b and c. If $\gamma_p < \gamma_M$, then $\Delta V = d\Delta A = 0.5d^3(\gamma_M - \gamma_p)$, Fig. 3b, and $\tau_B = G_M f(\gamma_M - \gamma_p)$ (assuming the GNDs are still stored in the matrix material). Similarly, if the strain in the particle is greater than that in the matrix, i.e. $\gamma_p > \gamma_M$ in Fig. 3c, it is $\Delta V = d\Delta A = 0.5d^3(\gamma_p - \gamma_M)$ and $\tau_B = G_M f(\gamma_p - \gamma_M)$. Ashby's relation can then be generalised for deformable particles in terms of the strain difference between the two phases as:

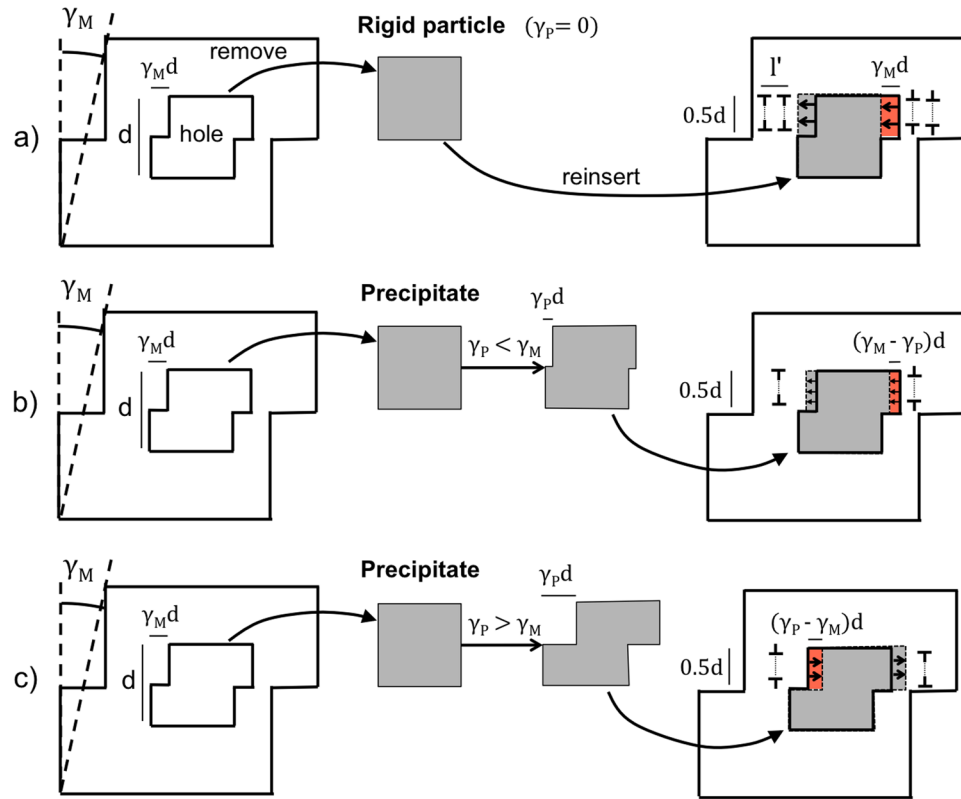


Figure 3. Diagram illustrating the three-steps abstraction of 1-removing the particle, 2- allowing the matrix to deform freely (intermediate configuration) and 3- reinserting the particle to derive a compatible arrangement of GNDs. (a) Case for a rigid particle, as in Ashby¹². (b) A precipitate shearing less than the matrix. (c) A precipitate shearing more than the matrix.

$$\tau_B = G_M f |\gamma_M - \gamma_P| \quad (5)$$

Setting $\gamma_P = 0$ recovers the case of a non-deformable particle.

In DIC experiments, the expression for the maximum shear strain is used, as mentioned above and detailed in the Methods section. Moreover, the strain of a given particle or matrix region is obtained as an average of the values measured within their respective domains. Hence, we rewrite Equation 5 as:

$$\tau_B = |G_M f \langle \gamma_{max}^M \rangle - \langle \gamma_{max}^P \rangle| = G_M f |p_{plastic}| \quad (6)$$

Inserting the values of $G_M f$ and $p_{plastic}$ in Table 1 into Equation 6 gives $\tau_B = 263$ MPa for CMSX-4 and about three times this value, $\tau_B = 772$ MPa, for the Fe-Ni₂AlTi.

Estimating relatively low back stresses for CMSX-4 is consistent with the 20% elongation that this can achieve at room temperature⁴⁶. On the other hand, the relatively high value obtained for Fe-Ni₂AlTi material, which may contribute to provide creep resistance at high temperatures as plastic deformation is confined to the matrix, is consistent with its poor ductility. In fact, although exhibiting strengths characteristic of the strongest steels, as shown above, the “as received” Fe-Ni₂AlTi microstructure does not possess the unique combination of high strength and good ductility that defines the emerging class of so-called ultrastrong (precipitate-strengthened) steels^{6,10,11}.

A Ductile Fe-Ni₂AlTi Microstructure

The finite element method (FEM)⁴⁷ is used to solve the partial differential equations (PDEs) governing the plasticity problem in domains that can be geometrically complex, such as the volume occupied by real particles. Crystal plasticity finite element (CP-FE) calculations, in particular, allow restricting the shear deformation along slip planes and directions and the modelling of the strain hardening associated with the accumulation of dislocations in the crystal lattice⁴⁸. Here, CP-FE analysis is used to gain a preliminary understanding of the factors influencing the evolution of $p_{plastic}$. To this end, we consider the compression of a precipitate-matrix unit volume of the Fe-Ni₂AlTi microstructure. Our CP-FE calculations are based on the conventional elastoplastic rate-dependent formulation⁴⁹. The Methods section provides details of the FE model and set-up. Predictions of Von Mises strains and stresses and the variation of $p_{plastic}$ are shown in Fig. 4a and b, respectively. During the initial elastic loading, $p_{plastic}$ is negative because the ferritic matrix is stiffer than the Ni₂AlTi precipitate (values of the elastic constants and hardening parameters are provided in Methods). The matrix then yields and its deformation

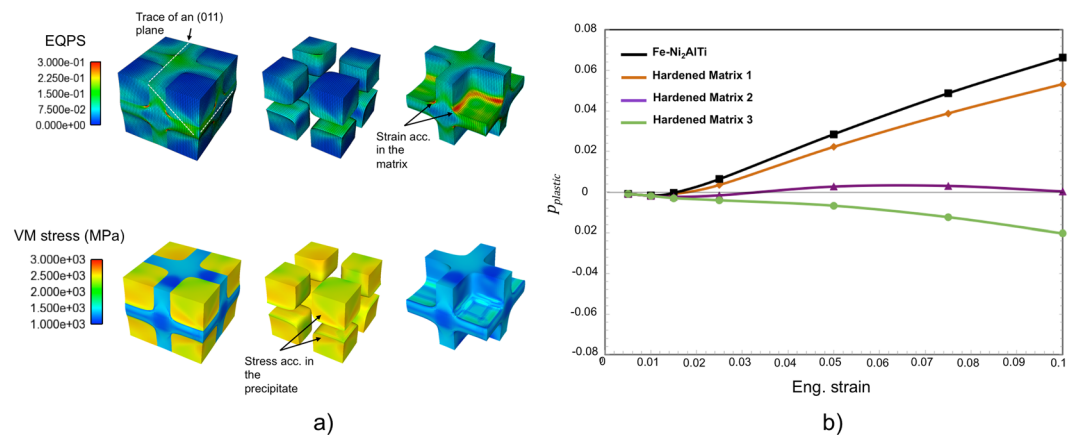


Figure 4. CP-FE simulations. (a) Top: von Mises strain (also known as the equivalent plastic strain EQPS) at 0.1 compressive strain shows bands along the {011} planes that cross the edge of the precipitate where strains of ~ 0.3 accumulate in the matrix. Bottom: von Mises stresses of $\sim 2.5 \times 10^3$ MPa build up at the interface as well and yet on the side of the precipitate. (b) Variation of $p_{plastic}$ in the Fe-Ni₂AlTi (precipitate-matrix) microstructure.

at the interface with the precipitate forces this to continue straining elastically. Consequently, $p_{plastic}$ turns positive as plastic strain accumulates in the matrix while stress does so in the precipitate, Fig. 4a. Eventually, the precipitate yields. However, plastic deformation is limited to its edges so that the value of $p_{plastic}$ keeps rising almost linearly with the applied strain, Fig. 4b.

Increasing the strain hardening rate of the matrix material (as well as softening the Ni₂AlTi phase) is predicted to bring forward precipitate shearing, leading to a decrease in the extent of plastic strain partitioning. This is shown in the same plot in Fig. 4b by the $p_{plastic}$ curves (Hardened Matrix 1–3) obtained after having increased the values of the hardening parameters for the ferritic matrix.

A way of softening the precipitates is to reduce the coherency stresses associated with the lattice misfit at the precipitate-matrix interfaces, as this makes it easier for the dislocations in the matrix to reach the interfaces and enter the precipitates⁵⁰. On the other hand, a way of increasing the rate of strain hardening in the matrix is to increase the number density of precipitates, as this proportionally increase the number of obstacles that the dislocations in the matrix need to overcome⁵¹.

Addition of Mo is known to reduce the lattice misfit and together decrease the size and spacing between the precipitates in the steel⁵². In the present study, the Fe-Ni₂AlTi steel was alloyed with 1.5 at.% and 5 at.% Mo. Adding Mo led to the formation of an additional Mo-rich hard phase. Lower Mo contents (1.4 at.% and 3.3 at.%, respectively) were therefore found at the length scale of the precipitate-matrix microstructure, where Mo accumulated in the matrix. The reduced values of the precipitates size and spacing and in the lattice misfit are given in Table 1.

The mappings of γ_{max} in compressed micropillars of +1.4 at.% and +3.3 at.% Mo are shown in Fig. 5a and b, respectively. In both cases, the spacing between slip bands is seen to decrease to the value measured earlier in the ferritic matrix micropillar. Also, there are no regions where high strains accumulate in the matrix as observed in the Mo-free microstructure. In fact, $p_{plastic}$ is found to decrease to 0.0020 in the +1.4 at.% Mo and -0.0006 in the +3.3 at.% Mo, see plot in Fig. 5c. The decrease in plastic strain partitioning did not affect the strengthening provided by the precipitate phase, as shown in the stress-strain curves of the compression tests in Fig. 5d.

Assuming that Mo addition has a negligible effect on G_M , substituting the values of $p_{plastic}$ and f (Table 1) into Equation 6 gives $\tau_B = 108$ MPa for the +1.4 at.% Mo and $\tau_B = 31$ MPa for the +3.3 at.% Mo, indicating that the rate at which the back stresses build up has been lowered. As discussed above, this would prevent early cavitation and cracking in the precipitate-matrix material under tensile loads. To demonstrate this, it is necessary to compare the response of the Mo-free and Mo added alloys to tensile stresses. Here, we use an indirect microtensile testing method^{53,54} in which microbeams are deflected at the centre while clamped at the extremes. The beams therefore elongates during deflection causing an axial tensile stress state to superimpose onto the one associated with pure bending. The three most stressed regions are located at the clamped ends and at the centre, as shown in Fig. 6a. If the cross-section of the beams is constant, however, the milled edges at the ends would act as stress concentrators, causing early damage. The bowtie geometry illustrated in Fig. 6a is therefore adopted to reduce the tensile stresses at the extremes and ensure these build up at the central-bottom region. The technique can then be used to compare the ductility of different materials by estimating the difference in the plastic strain that accumulates in such region before this cracks.

In the case of the +3.3% Mo, the relatively small spacing between the dendrites of the additional Mo-rich phase prevented the testing of microbeams free from hard masses. Being large non-deformable and brittle particles, these led to premature failure of the microbeams. For this reason, only the results of the Mo-free and the +1.4 at.% Mo tests are described hereafter. Results are shown in Fig. 6b–e and videos captured *in-situ* supplied as Supplementary Video S1 and Supplementary Video S2.

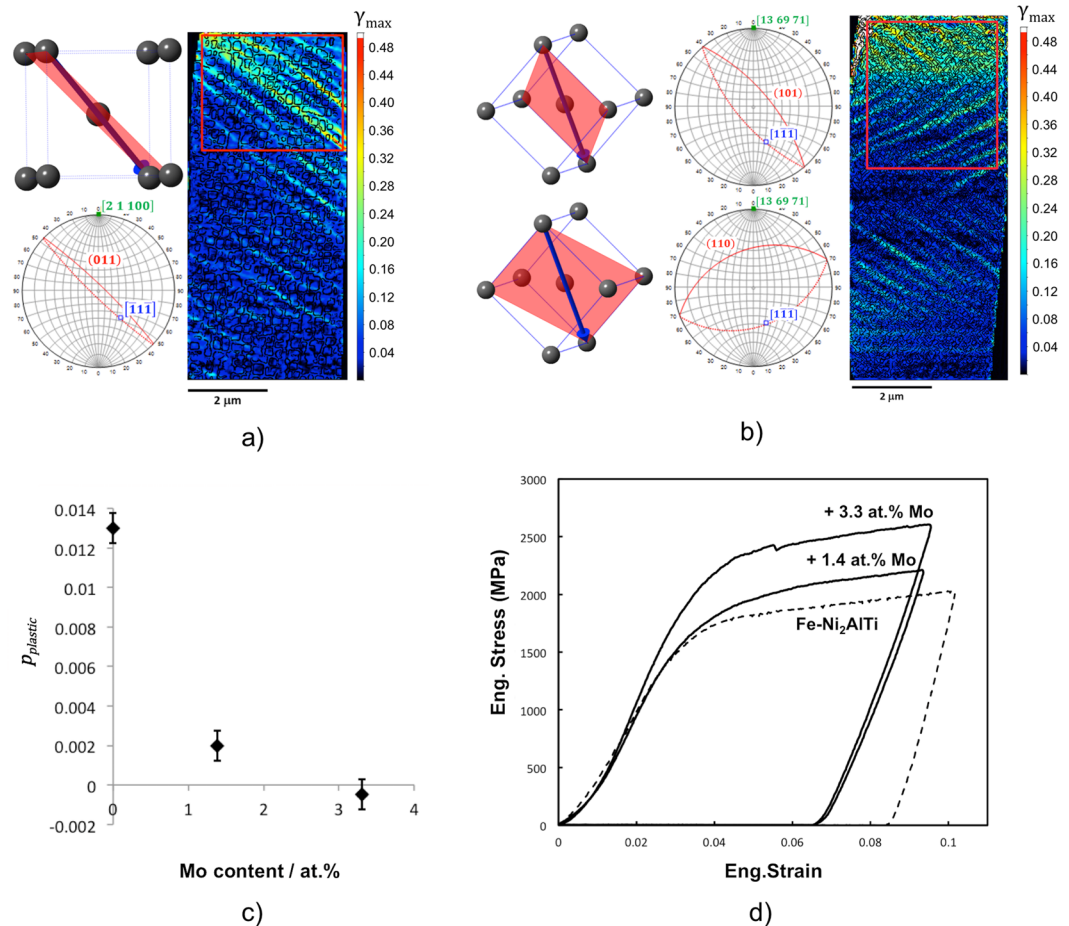


Figure 5. (a and b) Maximum shear strain maps of the Fe-Ni₂AlTi micropillars with 1.4 at.% and 3.3 at.% added Mo and with the precipitates outlined. The red lines outline the areas for which $p_{plastic}$ has been measured. Unit cells and stereograms show the crystallographic orientation and active slip systems in each pillar. The compression axis is shown in green, the slip planes in red and the slip directions in blue. (c) The decrease of $p_{plastic}$ with Mo content (d) Stress-strain curves of the compression tests to a nominal compressive strain of 0.1 showing that the high strength of the precipitate-matrix material is maintained.

In the Mo-free microbeam, cracking occurs in the central region of maximum tensile stresses, as expected, Fig. 6b. A single crack initiates at $\sim 3.5 \mu\text{m}$ deflection causing a small load drop in the load-deflection curve, point 2 in Fig. 6d, and grows gradually through discrete steps that produce further load drops, points 3, 4 and 5 in the same curve. The crack path is sometimes seen to circumvent the precipitates as in those highlighted by arrows in Fig. 6e (Detail A). A second crack later appears in the tensile zone at the left end of the microbeam (Detail B). In contrast, in the tensile regions of the +1.4 at.% Mo microbeam, sharp slip bands develop which are seen to cut through the precipitates, as shown in Fig. 6e (Details C and D). Cracking initiates only at $\sim 8.4 \mu\text{m}$ deflection and at 30% higher loads, Fig. 6d. In particular, two cracks are seen to grow along parallel slip bands and stop at the intersection with other (transversal) slip bands, (Detail C), suggesting that the plastic strain that accumulates in the latter has prevented stress localisation ahead of the crack tips.

As volume is conserved during plastic deformation, the accumulation of plastic strain in the central region of maximum axial tensile stresses must be accompanied by a reduction in the cross-section of the beam. This local reduction is not appreciable in the post-mortem SEM images of the Mo-free microbeam, indicating that the residual (axial) plastic strain of the region as a whole is below 0.01. In fact, the length of the bottom part of the microbeam highlighted in Fig. 6b (red line) coincides with its initial length (blue line). In the +1.4 at.% Mo microbeam, the transversal shrinkage is instead significant enough to cause a noticeable flattening of the bottom surface of the beam over a distance of approximately $10 \mu\text{m}$, as indicated in Fig. 6c. As the microbeam permanent elongation of $0.8 \pm 0.1 \mu\text{m}$ occurs along this length, the axial strain, ε_{axial} in the region is of the order of:

$$\varepsilon_{axial} = \frac{l - l_0}{l_0} = \frac{10 - 9.2}{9.2} \simeq 0.09 \quad (7)$$

This demonstrates that the Fe-Ni₂AlTi precipitate-matrix microstructure has acquired the capability of deforming plastically under tensile loads.

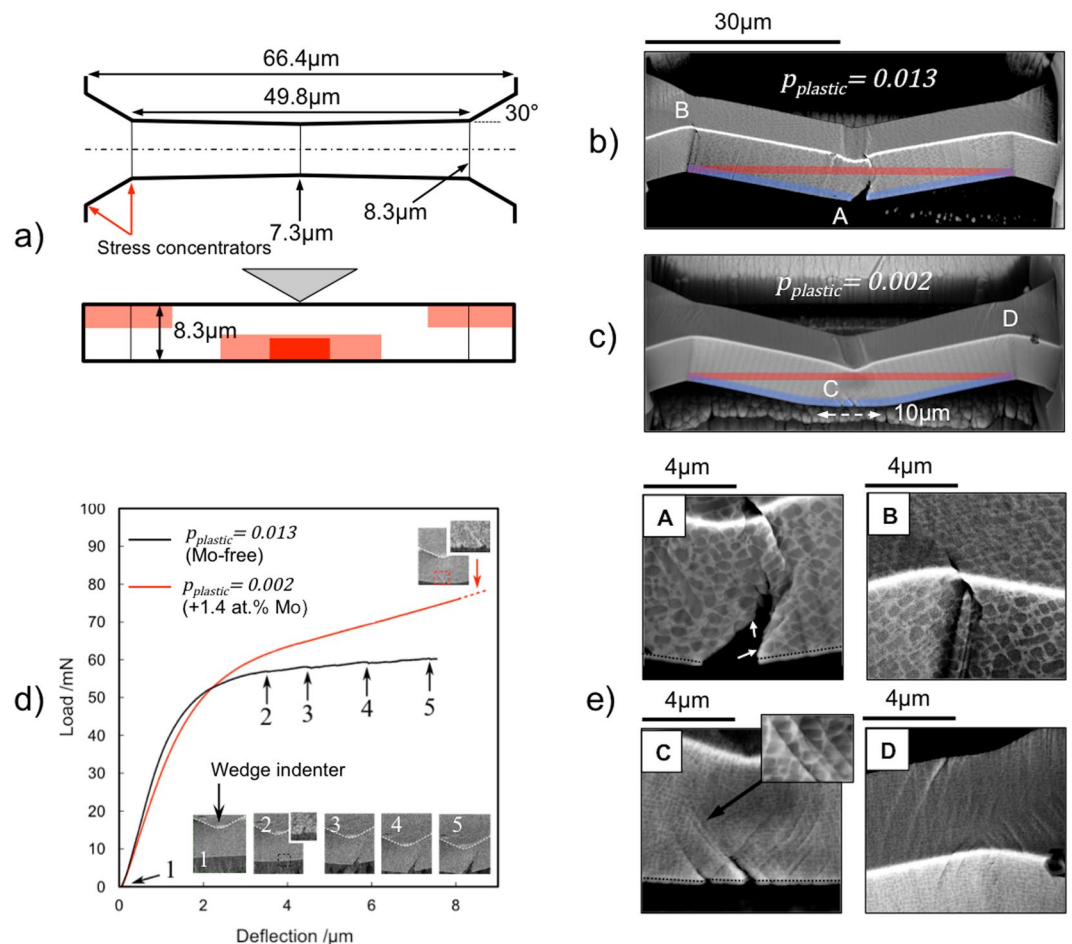


Figure 6. Microbeams bending tests. **(a)** Top and side view of the bowtie geometry. Red areas indicate the regions of maximum tensile stresses. **(b and c)** Post-mortem backscatter images acquired at a 52° tilt of the Mo-free and +1.4 at.% Mo microbeams, respectively. Thick lines highlight the differences in length of the bottom region of the microbeams before (red) and after (blue) deformation. **(d)** Compliance-corrected load-deflection curves with inset taken from video frames showing the initiation and propagation of the cracks. **(e)** Details of the backscatter images. (Top) Mo-free. (Bottom) +1.4 at.% Mo showing slip banding. The dashed lines at the bottom edges underline the pulverised material deposited here during the final milling step.

Summary and Outlook

We have shown that strain mapping using nanoscale digital image correlation enables the plastic strain difference between the matrix and the precipitate phases in precipitate-strengthened alloys to be measured. We have then extended the Ashby model to shearable particle so that the measurement of this strain difference, $p_{plastic}$, could be used to estimate the back stresses at the surface of the precipitates. Their build-up promotes cavitation and leads to premature failure under tensile loads. Consistent with this, we found these stresses to accumulate more rapidly in the Fe-Ni₂AlTi (precipitate-matrix) microstructure than in the one of the more ductile Ni-based superalloy CMSX-4. With the help of crystal plasticity calculations, we then aimed at finding ways to improve the mechanical behaviour of the former by controlling the value of $p_{plastic}$. This was achieved without loss in precipitate strengthening by decreasing the lattice misfit between the matrix and the precipitates and, at the same time, increasing the number density of precipitates. We then provided evidence of the enhanced ability of the new Fe-Ni₂AlTi microstructure to deform plastically under tensile stresses.

A significant increase in failure strains (to ~8% elongation) has been recently observed in precipitate-strengthened maraging steels following the minimisation of lattice misfit and the reduction of the precipitate size and spacing to few nanometres⁶. As the strength was retained, a unique combination of high strength and good ductility was obtained. The authors of the latter study considered the link between this specific microstructure and the exceptional mechanical properties to be counterintuitive. Here, we have demonstrated otherwise.

Moreover, our study indicates that reducing lattice misfit and the precipitate size and spacing might not be the only way to create a very strong and yet ductile precipitate-matrix microstructure. The mechanical response of each phase is in fact controlled by a multitude of other physical quantities, such as the antiphase boundary energy in the precipitate phase or the lattice resistance in the matrix phase³⁸. These are often difficult to measure and control without affecting other microstructural parameters. Measuring a sufficiently low $p_{plastic}$ at low

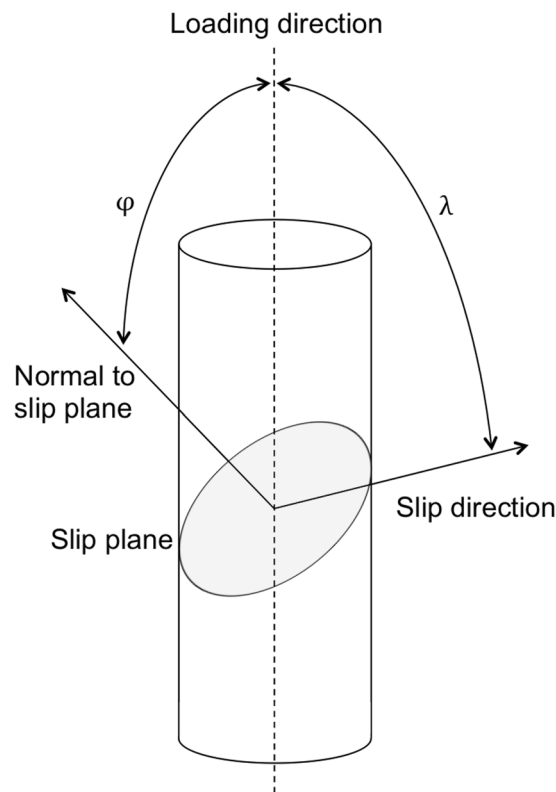


Figure 7. Angles considered in the calculation of the Schmid factor.

temperatures therefore emerges as the way in which one can verify that the above variables have been appropriately balanced to enhance the ductility of the precipitate-matrix microstructure.

Methods

Sample preparation and characterisation. The CMSX-4 samples, supplied by Rolls-Royce plc, were heat treated for eight hours at 1314 °C, followed by ageing for four hours at 1140 °C and then 16 hours 870 °C. The Ni₂AlTi-strengthened ferritic alloy, with a nominal composition Fe-20Ni-13.5Al-13.5Ti (at.%), was prepared by vacuum arc-melting. The bar of material was turned and re-melted a further five times to ensure the composition was homogeneous. The sample was then solution treated under vacuum at 1200 °C for two hours before being water quenched to room temperature. Vacuum arc-melting was also used to prepare the ferritic matrix-only sample with nominal composition Fe-6.5Ni-3.8Al-4.5Ti (at.%) and the alloys with added Mo. The compositions of these materials were verified by energy dispersive X-ray spectroscopy (EDX).

The average size, spacing and volume fraction of the precipitates were estimated from backscatter electron (BE) images of the microstructures using the mean lineal intercept of the precipitates and the mean free path between precipitates. Five large areas micrographs of each sample were considered. The results were in line with those obtained for the pillars, supporting the assumption that the microstructural parameters did not vary significantly into their depth.

Because of the cubic shape of the Ni₃Al precipitates in the CMSX-4, the BE images of the sides of the samples parallel to the {001} planes were used. The misfit between the matrix and the coherent precipitates for the Fe-Ni₂AlTi alloys was measured by X-ray diffraction (XRD). Each peak was individually fitted and then used for a least squares linear regression to determine the lattice parameter of each phase. Details can be found in Jones⁵⁵.

Micromechanical testing. *EBSD measurements.* Electron backscatter diffraction (EBSD) mapping was used to sample the crystallographic orientation at the edge of the samples where micropillars were to be milled. The locations chosen were those expected to give the least amount of out-of-plane slip, having considered the orientation of the slip system most likely to activate during microcompression. After testing, the crystallographic orientation was used to measure the angle between the slip planes and the plane of investigation in the calculations of the slip band spacing and to derive the critical resolved shear stress, as:

$$\tau_c = m_{\max} \times \sigma_y \quad (8)$$

where σ_y is the yield stress and m_{\max} the maximum value of the Schmid factor $m = \cos \varphi \cos \lambda$. As illustrated in Fig. 7, φ is the angle between the loading direction and the normal to the slip plane and λ is the angle between the loading direction and the slip direction. The {111}⟨011⟩ slip systems for CMSX-4 and the {011}⟨111⟩ slip systems for the ferritic steel were considered in the calculation of m_{\max} . The values of the above quantities are given in Table 2.

Alloy	Loading direction	φ (°)	λ (°)	m_{max}	σ_y (MPa)	τ_c (MPa)
CMSX-4 [010]	[0 1 0]	54.7	45	0.408	1000	410
CMSX-4 [011]	[8 61 79]	40.4	52.1	0.468	1100	510
Fe-Ni ₂ AlTi	[56 4 83]	52.1	38.9	0.478	1500	720
+1.4 at.% Mo	[2 1 100]	44.4	54.3	0.416	1600	670
+3.3 at.% Mo	[13 69 71]	53.5	42.8	0.437	2300	1000
Ferritic matrix	[25 15 96]	51.8	38.5	0.484	1000	480

Table 2. Values used in the calculation of the critical resolved shear stresses.

Voltage/kV	Current/nA	Dwell time/ μ s	Passes/No.	Duration/s	Beam size/nm
15	1.4	1200	1	43	13.3

Table 3. Electron beam deposition settings.

Voltage/kV	Current/nA	WD/mm	Scan time/min	Image size/pixels	Res/nm
15	1.4	4	6.1	2048 \times 1768	~5

Table 4. SEM imaging settings.

Micropillar preparation. Square section pillars with a side length of 5 μ m and an aspect ratio of approximately 1:3 were milled at the edge of each sample, using a focussed ion beam scanning electron microscope (FIB SEM) (Helios Nanolab, FEI, USA). The pillar was positioned ~5 μ m from the edge of the sample to avoid any overhang. Initially, the material was milled rapidly, at a current of 9 nA and an accelerating voltage of 30 kV, to shape the pillar and remove surrounding material. The final step involved a cleaning cross-section at 0.43 nA and a 2° offset from the vertical to remove any taper. The face on which the pattern was to be deposited was milled last, at a current of 0.23 nA, to reduce Ga+ implantation and re-deposition from the FIB milling. Finally, the sample was orientated so that the top of the pillar could be milled, to ensure it was flat and normal to the pillar axis. The above milling sequence helps minimise the effect that tapering and ion damage have on the observed strain hardening, an effect which is nevertheless expected to be negligible for the relatively large pillars tested here^{56,57}.

Speckle patterning. With the sample orientated so that the face for Pt deposition was normal to the electron beam, the speckle pattern was reproduced from the bitmap image provided in Di Gioacchino and Clegg¹⁷. The pattern, containing 4000 speckles of 3 \times 3 pixels, was deposited at the top of the pillar over an area of 4 \times 8 μ m². The deposition was completed in a single pass to avoid the spreading of deposited material that follows possible shifts in beam position due to sample charging. The amount of material deposited per point was controlled by the dwell time and was chosen to produce speckles ~40 nm in diameter. The conditions used are given in Table 3.

Micropillar testing. An image was acquired before compression, using the settings in Table 4. Microcompression was then carried out with an *in situ* nanoindenter using a 10 μ m flat punch (Alemnis, CH) in a field emission gun scanning electron microscope (FEG SEM) (Cross beam, Zeiss, GE). The punch was brought into proximity with the pillar and the latter compressed to ~0.1 strain with a nominal rate of 5 \times 10⁻³ s⁻¹. An image of the deformed pillar was taken in the original FIB-SEM microscope under the same conditions for DIC.

Microbeam preparation and testing. The same FIB SEM used for fabricating the micropillars was used to mill the bowtie-shaped microbeams. After an initial cut at 21 nA, four milling steps at 2 nA were alternated between the top and side to minimise the (re)deposition of the pulverized material on the edges of the beams. The microbeams were deflected at the centre at a nominal rate of 0.1 μ m s⁻¹ using a 10 μ m long wedge-shaped tip oriented transversally to the beam.

Strain mapping. Digital image correlation was carried out using commercial software (DaVis, LaVision, Germany), using subsets (S) down to 16 \times 16 pixels giving a spatial resolution of up to 80 \times 80 nm², with a window overlap of 50%. The image of the deformed pillar was correlated with the undeformed pillar image to obtain the 2D displacement field on the *xy* plane of investigation. This was used to calculate the maximum shear strain, γ_{max} at each subset:

$$\gamma_{max}(S) = 2 \cdot \sqrt{\left(\frac{\epsilon_{xx} - \epsilon_{yy}}{2}\right)^2 + \left(\frac{\gamma_{xy}}{2}\right)^2} \quad (9)$$

where ϵ_{xx} , ϵ_{yy} and $\gamma_{xy} = 2\epsilon_{xy} = \epsilon_{yx}$ are the strain components in the *xy* plane. Note that γ_{max} is sometimes defined as the square root term alone.

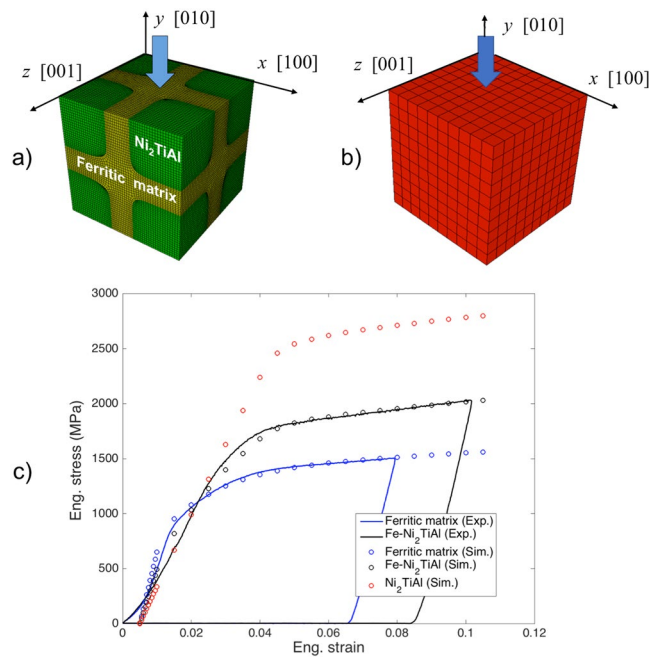


Figure 8. (a) Two-phases FE model used to represent a unit volume of the Fe-Ni₂AlTi microstructure. (b) Single-phase FE model. (c) Fitting of the experimental stress-strain curves (ferritic matrix-only and Fe-Ni₂AlTi micropillars) and predicted mechanical response of the Ni₂AlTi precipitate phase.

In the case of simple shear depicted in Fig. 3 to illustrate the Ashby model, in which the slip direction is in the xy plane, $\varepsilon_{xx} - \varepsilon_{yy} = 0$ and hence $\gamma_{max} \equiv \gamma_{xy}$. As described above, the crystallographic orientations of the micropillars were chosen as to minimise out-of-plane slip. Nevertheless, where the latter occurs, it would manifest in the DIC measurements as an apparent in-plane stretch (or compression), i.e. generally $\varepsilon_{xx} - \varepsilon_{yy} \neq 0$. Therefore, the expression for γ_{max} in Equation 9 has been used here and in previous high-resolution DIC studies^{26,33,58} because it compensates for the lack of out-of-plane displacement data.

Two images of the same speckle pattern acquired at the conditions used for testing were correlated to characterise the spatial distortion associated with irregularities in the SEM scan. The correlation produced a bundle of horizontal bands of ~ 0.04 strain in the γ_{max} map. Therefore, each individual value had an error of $\delta = \pm 0.04$.

Splitting of the strain data. Images of the pillars used for DIC also displayed compositional contrast, as shown in Fig. 1. This enabled the positions of the precipitates to be identified and outlined directly on the maps of maximum shear strain. The outlining was done by inspection by eye and thresholding on the ImageJ software (National Institute of Health, USA). The value of $\langle \gamma_{max}^P \rangle$ was determined by summing the maximum shear strain values obtained for the precipitate phase (P) using Equation 9 and dividing by the number of data points, N^P :

$$\langle \gamma_{max}^P \rangle = \frac{\sum_{S \in P} \gamma_{max}(S)}{N^P} \quad (10)$$

The same was done to calculate $\langle \gamma_{max}^M \rangle$.

The standard error in the mean shear strain was then calculated as $S. E. = \delta / \sqrt{n}$, where n is the number of shear strain values used to calculate the mean. For each phase, the mean shear strain was calculated from a large number shear strain values (> 2000) and therefore the corresponding error was relatively small < 0.0008 . Despite this uncertainty, it is important to note that the sign of the calculated $p_{plastic}$ remains unaffected.

CPFEM: meshing, boundary conditions and calibration. The finite elements domain considered in the present study is a cube having one-eighth of a precipitate in each corner and the faces parallel to the {001} directions, Fig. 8a. The cuboidal precipitate was reproduced by 163,400 hexahedral finite elements, and the smooth interfaces between two phases were constructed while maintaining precipitate volume fraction of 50.6%⁵⁹. Taking an orthogonal (x, y, z) coordinate system with origin at a top corner of the cube and axes normal to its faces, as shown in the same figure, the compression was applied with a rate of $1 \times 10^{-3} \text{ s}^{-1}$ by displacing the $y = 0$ face along $-y$ direction while imposing $u_x = 0$ on the $x = 0$ face, $u_z = 0$ on the $z = 0$ face and $u_y = 0$ on the $-y$ face. The {011}⟨111⟩ slip systems were considered. No initial internal stresses were imposed at the precipitate-matrix interface.

The slip rate on each slip system was represented as a power-law function of the resolved shear stress. A dislocation density based hardening was also adopted^{60,61}. The hardening parameter, g , has the expression:

	k_1	k_2	C_{11}/GPa	C_{12}/GPa	C_{44}/GPa	b/mm
Ni ₂ AlTi	1.5×10^8	3×10^2	152.0	103.9	94.0	2.29×10^{-7}
Fe Matrix	1×10^8	3.5×10^2	228.0	132.0	116.5	2.48×10^{-7}
Matrix 1	1.4×10^8	3.5×10^2	"	"	"	"
Matrix 2	5×10^8	3.5×10^2	"	"	"	"
Matrix 3	2×10^9	1×10^3	"	"	"	"

Table 5. Values of the parameters used in the CP-FE analysis.

$$g = AGb \sqrt{\sum_{\alpha=1}^N \rho^\alpha} \quad (11)$$

where A is a material constant, G is the shear modulus, b is the Burger's vector and ρ^α is the dislocation density in α -th slip system. The evolution of dislocation density is then obtained by a standard phenomenological equation,

$$\dot{\rho}^\alpha = \left(k_1 \sum_{\beta=1}^N \rho^\beta - k_2 \rho^\alpha \right) \cdot |\dot{\gamma}^\alpha| \quad (12)$$

where, k_1 and k_2 control the generation and annihilation of dislocations, respectively.

In the present study, values of k_1 and k_2 for the matrix phase were acquired by fitting the stress-strain curve predicted for a "single phase" cuboid, Fig. 8b, to the curve obtained for the ferritic matrix micropillar. The hardening parameters for the Ni₂AlTi phase were then adjusted to make the stress-strain curve predicted for the "two phases" FE cuboid match that of the Fe-Ni₂AlTi micropillar. The two fitted stress-strain curves and the one predicted for the Ni₂AlTi material are shown in Fig. 8c.

The values of the parameters used for the CP-FE calculations are reported in Table 5.

References

- Pollock, T. M. & Tin, S. Nickel-based superalloys for advanced turbine engines: chemistry, microstructure and properties. *J. Propuls. Power* **22**, 361–374 (2006).
- Pollock, T. M. Alloy design for aircraft engines. *Nat. Mater.* **15**, 809–815 (2016).
- Sato, J. *et al.* Cobalt-base high-temperature alloys. *Science* **312**, 90–91 (2006).
- Sun, Z. *et al.* New design aspects of creep-resistant NiAl-strengthened ferritic alloys. *Scr. Mater.* **68**, 384–388 (2013).
- Darolia, R. NiAl alloys for high-temperature structural applications. *JOM* **43**, 44–49 (1991).
- Jiang, S. *et al.* Ultrastrong steel via minimal lattice misfit and high-density nanoprecipitation. *Nature* **544**, 460–464 (2017).
- Nie, J. Precipitation and hardening in magnesium alloys. *Metall. Mater. Trans. A* **43A**, 3891–3939 (2012).
- Jia, N. *et al.* Nanoscale spheroidized cementite induced ultrahigh strength-ductility combination in innovatively processed ultrafine-grained low alloy medium-carbon steel. *Sci. Rep.* **7** (2017).
- Song, G. *et al.* Ferritic alloys with extreme creep resistance via coherent hierarchical precipitates. *Sci. Rep.* **5**, 16327 (2015).
- Kim, S.-H., Kim, H. & Kim, N. J. Brittle intermetallic compound makes ultrastrong low-density steel with large ductility. *Nature* **518**, 77–79 (2014).
- Raabe, D., Ponge, D., Dmitrieva, O. & Sander, B. Nanoprecipitate-hardened 1.5 GPa steels with unexpected high ductility. *Scr. Mater.* **60**, 1141–1144 (2009).
- Ashby, M. F. The deformation of plastically non-homogeneous materials. *Philos. Mag.* **21**, 399–424 (1970).
- Humphreys, J. & Bate, P. Gradient plasticity and deformation structures around inclusions. *Scr. Mater.* **48**, 173–178 (2003).
- Ashby, M. F. Work hardening of dispersion-hardened crystals. *Philos. Mag.* **132**, 1157–1178 (1966).
- Ma, S., Rangaswamy, P. & Majumdar, B. S. Microstress evolution during *in situ* loading of a superalloy containing high volume fraction of gamma prime phase. *Scr. Mater.* **48**, 525–530 (2003).
- Daymond, M. R., Preuss, M. & Clausen, B. Evidence of variation in slip mode in a polycrystalline nickel-base superalloy with change in temperature from neutron diffraction strain measurements. *Acta Mater.* **55**, 3089–3102 (2007).
- Coakley, J. & Dye, D. Lattice strain evolution in a high volume fraction polycrystal nickel superalloy. *Scr. Mater.* **67**, 435–438 (2012).
- Huang, S. *et al.* Deformation mechanisms in a precipitation-strengthened ferritic superalloy revealed by *in situ* neutron diffraction studies at elevated temperatures. *Acta Mater.* **83**, 137–148 (2015).
- Sun, Z. *et al.* Load partitioning between the bcc-iron matrix and NiAl-type precipitates in a ferritic alloy on multiple length scales. *Sci. Rep.* **6**, 1–9 (2016).
- Coakley, J. *et al.* Lattice strain evolution and load partitioning during creep of a Ni-based superalloy single crystal with rafted γ' microstructure. *Acta Mater.* **135**, 77–87 (2017).
- Ritchie, R. O. The conflicts between strength and toughness. *Nat. Mater.* **10**, 817–822 (2011).
- Bruck, H. A., McNeill, S. R., Sutton, M. A. & Peters, W. H. Digital image correlation using Newton-Raphson method of partial differential correction. *Exp. Mech.* **29**, 261–267 (1989).
- Ososkov, Y., Wilkinson, D. S., Jain, M. & Simpson, T. *In-situ* measurement of local strain partitioning in a commercial dual-phase steel. *Int. J. Mat. Res.* **98** (2007).
- Han, Q., Kang, Y., Hodgson, P. D. & Stanford, N. Quantitative measurement of strain partitioning and slip systems in a dual-phase steel. *Scr. Mater.* **69**, 13–16 (2013).
- Tasan, C. C. *et al.* Integrated experimental-simulation analysis of stress and strain partitioning in multiphase alloys. *Acta Mater.* **81**, 386–400 (2014).
- Di Gioacchino, F. & da Fonseca, J. Q. An experimental study of the polycrystalline plasticity of austenitic stainless steel. *Int. J. Plast.* **74**, 92–109 (2015).
- Kamikawa, N. *et al.* Tensile behavior of ferrite-martensite dual phase steels with nano-precipitation of vanadium carbides. *ISIJ Int.* **55**, 1781–1790 (2015).
- Rnek, C. & Engelberg, D. L. An experimental investigation into strain and stress partitioning of duplex stainless steel using digital image correlation, X-ray diffraction and scanning Kelvin probe force microscopy. *J. Strain Anal.* **51**, 207–219 (2016).

29. Bettanini, A. M. *et al.* Influence of microscopic strain heterogeneity on the formability of martensitic stainless steel. In *AIP Conference Proceedings* **1896**, 20010 (AIP Publishing LLC 2017).
30. Fujita, N., Ishikawa, N., Roters, F., Tazan, C. C. & Raabe, D. Experimental–numerical study on strain and stress partitioning in bainitic steels with martensite–austenite constituents. *Int. J. Plast.*, <https://doi.org/10.1016/j.ijplas.2018.01.012> (2018).
31. Stinville, J. C. *et al.* Sub-grain scale digital image correlation by electron microscopy for polycrystalline materials during elastic and plastic deformation. *Exp. Mech.*, <https://doi.org/10.1007/s11340-015-0083-4> (2015).
32. Stinville, J. C., Vanderesse, N., Bridier, F., Bocher, P. & Pollock, T. M. Acta Materialia High resolution mapping of strain localization near twin boundaries in a nickel-based superalloy. *Acta Mater.* **98**, 29–42 (2015).
33. Di Gioacchino, F. & Quinta da Fonseca, J. Plastic strain mapping with sub-micron resolution using digital image correlation. *Exp. Mech.* **53**, 743–754 (2013).
34. Edwards, T. E. J., Di Gioacchino, F., Springbett, H. P., Oliver, R. A. & Clegg, W. J. Stable speckle patterns for nano-scale strain mapping up to 700 °C. *Exp. Mech.* 1–14, <https://doi.org/10.1007/s11340-017-0317-8> (2017).
35. Di Gioacchino, F. & Clegg, W. J. Mapping deformation in small-scale testing. *Acta Mater.* **78**, 103–113 (2014).
36. Edwards, T. E. J., Di Gioacchino, F., Muñoz-Moreno, R. & Clegg, W. J. Deformation of lamellar TiAl alloys by longitudinal twinning. *Scr. Mater.* **118**, 46–50 (2016).
37. Edwards, T. E. J. *et al.* Longitudinal twinning in a TiAl alloy at high temperature by *in situ* microcompression. *Acta Mater.*, <https://doi.org/10.1016/j.actamat.2018.01.007> (2018).
38. Meyers, M. A. & Chawla, K. K. *Mechanical behavior of materials* (Cambridge University Press, 2009).
39. Korte, S., Stearn, R. J., Wheeler, J. M. & Clegg, W. J. High temperature microcompression and nanoindentation in vacuum. *J. Mater. Res.* **27**, 167–176 (2012).
40. Bramfitt, B. L. In *Metals handbook Desk edition, Second Edition* 153–173 (1998).
41. Beardmore, P. & Davies, G. J. T. On the temperature dependence of the flow stress of nickel-based alloys. *Trans. Metall. Soc. AIME* **245**, 1537–2545 (1969).
42. Di Gioacchino, F. Characterization of mesoscopic crystal plasticity from high resolution surface displacement and lattice orientation mappings. *PhD Thesis* (The University of Manchester, Manchester, UK 2013).
43. da Fonseca, J. Q. & Ko, L. The kinematics of deformation and the development of substructure in the particle deformation zone. *IOP Conf. Ser. Mater. Sci. Eng.* **89**, 12012 (2015).
44. Nye, J. F. Some geometrical relations in dislocated crystals. *Acta Metall.* **1**, 153–162 (1953).
45. Brown, L. M. & Stobbs, W. M. The work-hardening of copper-silica v. equilibrium plastic relaxation by secondary dislocations. *Philos. Mag.* **34**, 351–372 (1976).
46. Sengupta, A. *et al.* Tensile behavior of a new single-crystal nickel-based superalloy (CMSX-4) at room and elevated temperatures. *J. Mater. Eng. Perform.* **3**, 73–81 (1994).
47. Zienkiewicz, O. C. & Taylor, R. L. (Robert L. *The finite element method*. (Butterworth-Heinemann, 2000).
48. Havner, K. S. *Finite plastic deformation of crystalline solids*. (Cambridge University Press, 1992).
49. Peirce, D., Asaro, R. J. & Needleman, A. An analysis of nonuniform and localized deformation in ductile single crystals. *Acta Metall.* **30**, 1087–1119 (1982).
50. Gao, S., Fivel, M., Ma, A. & Hartmaier, A. Influence of misfit stresses on dislocation glide in single crystal superalloys: A three-dimensional discrete dislocation dynamics study. *J. Mech. Phys. Solids* **76**, 276–290 (2015).
51. Huang, M., Zhao, L. & Tong, J. Discrete dislocation dynamics modelling of mechanical deformation of nickel-based single crystal superalloys. *Int. J. Plast.* **28**, 141–158 (2012).
52. Calderon, H. A., Fine, M. E. & Weertman, J. R. Coarsening and morphology of β' particles in Fe-Ni-Al-Mo ferritic alloys. *Metall. Trans. A* **19**, 1135–1146 (1988).
53. Gianola, D. S. & Eberl, C. Micro- and nanoscale tensile testing of materials. *JOM* **61**, 24–35 (2009).
54. Zhu, Y., Ke, C. & Espinosa, H. D. Experimental techniques for the mechanical characterization of one-dimensional nanostructures. *Exp. Mech.* **47**, 7–24 (2007).
55. Jones, R. D. Deformation in A2/B2 Alloys. *PhD Thesis* (University of Cambridge, 2016).
56. El-Awady, J. A., Woodward, C., Dimiduk, D. M. & Ghoniem, N. M. Effects of focused ion beam induced damage on the plasticity of micropillars. *Phys. Rev. B* **80**, 104104 (2009).
57. Kondori, B., Needleman, A. & Amine Benzerga, A. Discrete dislocation simulations of compression of tapered micropillars. *J. Mech. Phys. Solids* **101**, 223–234 (2017).
58. Orozco-Caballero, A., Lunt, D., Robson, J. D. & da Fonseca, J. Q. How magnesium accommodates local deformation incompatibility: a high-resolution digital image correlation study. *Acta Mater.* **133**, 367–379 (2017).
59. Lim, H. *et al.* Incorporating physically-based microstructures in materials modeling: Bridging phase field and crystal plasticity frameworks. *Model. Simul. Mater. Sci. Eng.* **24**, 45016 (2016).
60. Lee, M. G., Lim, H., Adams, B. L., Hirth, J. P. & Wagoner, R. H. A dislocation density-based single crystal constitutive equation. *Int. J. Plast.* **26**, 925–938 (2009).
61. Lim, H. *et al.* Grain-scale experimental validation of crystal plasticity finite element simulations of tantalum oligocrystals. *Int. J. Plast.* **60**, 1–18 (2014).

Acknowledgements

F.D., R.D.J., C.S. and W.J.C. acknowledge the support of the EPSRC/Rolls-Royce plc Strategic Partnership (EP/M005607/1). Sandia National Laboratories is a multimission laboratory managed and operated by National Technology and Engineering Solutions of Sandia LLC, a wholly owned subsidiary of Honeywell International Inc. for the U.S. Department of Energy's National Nuclear Security Administration under contract DE-NA0003525.

Author Contributions

F.D., R.D.J. and W.J.C. devised the study of the plastic strain partitioning in precipitate-matrix microstructures and drafted the paper. F.D. extended the Ashby model to shearable particles. R.D.J. prepared the samples, conducted the micropillar compression and analysed the experimental measurements. C.S. carried out the testing of the $\langle 001 \rangle$ -oriented CMSX-4 micropillar. F.D. and T.E.J.E. designed and carried out the microbeam bending tests. H.L. planned and conducted the crystal plasticity finite element simulations with contributions by C.C.B. All authors read and commented on the manuscript at all stages.

Additional Information

Supplementary information accompanies this paper at <https://doi.org/10.1038/s41598-018-26917-0>.

Competing Interests: The authors declare no competing interests.

Publisher's note: Springer Nature remains neutral with regard to jurisdictional claims in published maps and institutional affiliations.



Open Access This article is licensed under a Creative Commons Attribution 4.0 International License, which permits use, sharing, adaptation, distribution and reproduction in any medium or format, as long as you give appropriate credit to the original author(s) and the source, provide a link to the Creative Commons license, and indicate if changes were made. The images or other third party material in this article are included in the article's Creative Commons license, unless indicated otherwise in a credit line to the material. If material is not included in the article's Creative Commons license and your intended use is not permitted by statutory regulation or exceeds the permitted use, you will need to obtain permission directly from the copyright holder. To view a copy of this license, visit <http://creativecommons.org/licenses/by/4.0/>.

© The Author(s) 2018